

Reprocessed emission line profiles from dense clouds in geometrically thick accretion engines

Sean A. Hartnoll^{1,2} and Eric G. Blackman¹

¹ Department of Physics and Astronomy, University of Rochester, Rochester NY 14627, USA

² St. John's College, Cambridge University, Cambridge CB2 1TP, UK

Submitted version

ABSTRACT

The central engines of active galactic nuclei (AGN) contain cold, dense material as well as hot X-ray emitting gas. The standard paradigm for the engine geometry is a cold thin disc sandwiched between hot X-ray coronae. Strong support for this geometry in Seyferts comes from the study of fluorescent iron line profiles, although the evidence is not ubiquitously air tight. The thin disc model of line profiles in AGN and in X-ray binaries should be bench marked against other plausible possibilities. One proposed alternative is an engine consisting of dense clouds embedded in an optically thin, geometrically thick X-ray emitting engine. This model is further motivated by studies of geometrically thick engines such as advection dominated accretion flows (ADAFs). Here we compute the reprocessed iron line profiles from dense clouds embedded in geometrically thick, optically thin X-ray emitting discs near a Schwarzschild black hole. We consider a range of cloud distributions and disc solutions, including ADAFs, pure radial infall, and bipolar outflows. We find that such models can reproduce line profiles similar to those from geometrically thin, optically thick discs and might help alleviate some of the problems encountered from the latter.

Key words: accretion, accretion discs - line: profiles - line: formation - galaxies: active - galaxies: Seyfert - X-rays: galaxies

1 INTRODUCTION

Active galactic nuclei (AGN) and some X-ray binaries are thought to be powered by accretion onto massive black holes (e.g. Rees 1984; Tanaka 2000). Observations suggest that cold matter in the accretion engine reprocesses the primary X-ray continuum (e.g. George and Fabian 1991). In particular, a fluorescent iron K α emission line profile is imprinted on the spectrum near 6.4 keV. The iron line profile is shaped by Doppler and gravitational frequency shifts (Fabian et al. 1989), and hence contains information about geometry and dynamics in the innermost regions of the accretion engine (see Fabian et al. 2000 for a comprehensive review).

Most modelling of iron line profiles has been carried out within the paradigm of geometrically thin, optically thick discs. The initial flat disc model of Fabian et al. (1989) was generalised to Kerr black holes by Laor (1991). More recently, Pariev and Bromley (1998) have considered effects of a small disc thickness and turbulence.

Thin disc line profiles successfully reproduce many features in the experimental data (e.g. Tanaka et al. 1995; Nandra et al. 1997). However there are some observations which remain difficult to understand within this paradigm. For example, a preference for low inclinations, even amongst

Seyfert 2s (Turner et al. 1998), disagreements between the predicted inclination from iron line modelling and the predicted inclination from other phenomena (Nishiura et al. 1998; Sulentic et al. 1998a; Wang et al. 1999), and problems with the observed reprocessed fraction being too low or not correlated with line width (e.g. Lee et al. 2000; Chiang et al. 2000; Weaver 2000; Sulentic et al. 1998b).

Such puzzles may be resolved within the paradigm of thin discs, for instance by introducing additional emission components from an obscuring torus (Weaver and Reynolds 1998) or invoking flared or warped discs in which the inner and outer regions are not aligned (Blackman 1999; Hartnoll and Blackman 2000). In any case, alternative plausible geometries still merit exploration to provide proper diagnostics for comparison.

A particularly interesting alternative extends from work on the survival of cold clouds capable of reprocessing X-ray flux in the AGN engines (e.g. Ferland and Rees 1988; Guilbert and Rees 1988; Celotti, Fabian and Rees 1992). Physical constraints on the size of the dense clouds have been studied by Kuncic et al. (1996). They found a sizeable parameter regime in which cool, dense, small clouds can coexist with a hot medium in a dynamical equilibrium. Though X-ray continuum features of the embedded cloud model have

been studied by several authors (Sivron and Tsuruta 1993; Bond and Matsuoka 1993; Nandra and George 1994; Collin-Souffrin et al. 1996), detailed calculations of reprocessed line profiles have not been carried out. Karas et al. (2000) have studied line emission from reprocessing by a nearly spherical shell of clouds at a specific radius that results from a standard thin disc being disrupted due to instabilities. They give resulting line profiles from illumination by a central source. This is a different scenario from what we will consider here. Other related calculations of note include Cao and Zhang (1991), who calculated line profiles for radially infalling gas.

In this paper we calculate the (iron) line profiles that result from various distributions of small, cold clouds embedded in an optically thin, geometrically thick accretion disc or corona. As well as illumination from a central source, we include an illumination by an ‘X-ray bath’ of radiation; each cloud is taken to be small enough to be illuminated isotropically at their positional location by this bath component. This two component illumination is motivated from considering geometrical thick models such as, for example, advection dominated accretion flows (ADAFs) (e.g. Rees et al. 1982; Narayan and Yi 1994; see Narayan et al. 1998 for a review), which can be interpreted to have a synchrotron + Bremsstrahlung centrally dominated illumination (Madau 1997) and a Bremsstrahlung X-ray bath. Depending on the accretion rate of the disc, the synchrotron or Bremsstrahlung will dominate. ADAFs predict luminosities significantly less than the Eddington value L_E , and may just be applicable to Seyferts, with typical luminosities $L_E/100$.

We will use several flow solutions to prescribe a velocity field for the clouds; standard full ADAF solutions, pure radial infall, and bipolar outflows. The profiles calculated may also therefore be relevant for the dynamics of convection dominated accretion flows (CDAFs) (Quataert and Gruzinov 2000; Narayan et al. 2000), Advection Dominated Inflow Outflow Models (ADIOS) (Blandford and Begelman 1999) or other thick disc models. The microphysics of the direct X-ray line emission for ADAFs have been studied in non-relativistic flows (e.g. Narayan and Raymond 1999; Perna et al. 2000), but not the presence of cold reprocessing matter, nor the associated relativistic iron fluorescence line profiles. Like Karas et al. (2000), we take the clouds to be optically thick, and allow the clouds to shadow emission from other clouds.

Some profiles for relativistic outflows have been calculated by Wang et al. (2000). These outflows are different from those considered here in that they are pencil beams along the spin axis and not radial outflow in a geometrically thick disc. The spherical geometry, and covering by clouds, can avoid the large blue shifted component that has not been observed in iron lines and that is characteristic of outflows.

It has been suggested (e.g. Nandra 2000) that a geometrically thick distribution of clouds would result in more blue-shifted emission than is observed. The data from a variety of sources are also not inconsistent with a somewhat larger blue wing (Nandra et al. 1997). But we find that because models of geometrically thick discs can generally have smaller bulk velocities in the central regions than the flat disc keplerian velocities, smaller Doppler blue shifts result, and gravitational redshift becomes the dominant spectral feature. For these reasons also, the line profiles for thick discs will in general be less inclination dependent than those

from thin discs. This will be discussed in more detail below. It may help explain problems encountered with inclinations in thin disc modelling. When the velocities are faster, the profiles are very similar to the standard profiles obtained from thin disc modelling.

In section 2 we describe the disc model of dense clouds in geometrically thick discs. Section 3 contains the calculation of iron line profiles from this model. Section 4 presents the resulting line profiles and a discussion of the main features. Section 5 is the conclusion.

2 THE EMBEDDED CLOUD MODEL: DENSE CLOUDS AND THICK DISCS

The model consists of small optically thick clouds embedded in, and hence following, the fluid flow in an otherwise optically thin disc. Although the clouds may have a short lifetime, the continuous creation and destruction of clouds allows the definition of an effective number density of clouds at each point, $n_c(\mathbf{r})$. We consider these clouds to be both bathed in an locally isotropic radiative flux (e.g. Bremsstrahlung) and to be illuminated by a central source (e.g. synchrotron dominated). The clouds are assumed to be small compared to disc length scales (see Celotti et al. 1992 and Kuncic et al. 1996 for partial justification).

Calculating the profile then involves an optical depth calculation; we integrate the number density times the cross section along the photon trajectories to obtain a probability of obscuration. Contributions are integrated across the whole disc to obtain a profile, as is done for the usual thin disc, except that now we are integrating over three dimensions.

We consider several different solutions to the accretion flow involving optically thin, geometrically thick engines: self-similar ADAFs (Narayan and Yi 1995; Perna et al. 2000), bipolar outflows (Xu and Chen 1997; Perna et al. 2000), and radial infall (appendix B of Narayan and Yi 1995, similar to Bondi 1952).

2.1 self-similar ADAF

Self-similar accretion solutions are described in Narayan and Yi (1995). The approximate analytic solutions, given in Perna et al. (2000), for the density (ρ), velocities (v_r, v_θ, v_ϕ), and sound speed (c_s) are

$$\rho = \rho_0 r^{-\frac{3}{2}} [c_s^2(\theta)]^{-2.25}, \quad (1)$$

$$v_r = -\frac{3\alpha}{5+2\epsilon} r \Omega_K(r) \sin^2 \theta, \quad (2)$$

$$v_\theta = 0, \quad (3)$$

$$v_\phi = \left(\frac{2\epsilon}{5+2\epsilon} \right)^{\frac{1}{2}} r \Omega_K(r) \sin \theta, \quad (4)$$

$$c_s = r \Omega_K(r) \left[\frac{2}{5} - \left(\frac{2}{5} - \frac{2}{5+2\epsilon} \right) \sin^2 \theta \right]^{\frac{1}{2}}, \quad (5)$$

where $\Omega_K(r)$ is the Keplerian angular velocity, $\Omega_K(r) = r^{-\frac{3}{2}}$ in our units and we are using standard spherical polar coordinates, (r, θ, ϕ) .

There are two free parameters, the Sakura-Sunyaev viscosity parameter, α , and a thermodynamic parameter,

$$\epsilon = \left(\frac{5/3 - \gamma}{\gamma - 1} \right), \quad (6)$$

with γ the ratio of specific heats. We will consider $\alpha = 0.35$ and $\epsilon = 10, 0.1$. Solutions are taken to be in the fully advection dominated case. Note that:

- (i) Lower ϵ gives lower angular speeds.
- (ii) For $\epsilon = 10$ most of the matter is close to the equatorial plane, whilst for $\epsilon = 0.1$ the matter is essentially uniformly distributed in θ .
- (iii) For larger values of α , such the $\alpha = 0.35$ we consider, v_r is very similar to v_ϕ . For smaller α , the radial motion becomes less important.
- (iv) $c_s(\theta)$ is smaller on the equatorial plane and is smaller for larger ϵ . This will mean that, at fixed radius, the clouds are larger on the equatorial plane and larger in high ϵ cases.

2.2 Radial infall

The self-similar forms of the previous section admit a radially infalling solution (Narayan and Yi 1995, it is essentially Bondi accretion with viscosity.) We take the radial infall to be at the Keplerian velocity, $r\Omega_K(r)$, which implies that the sound speed is $c_s = \frac{r\Omega_K(r)}{\sqrt{5}}$. This solution corresponds to a small ϵ , and so represents a geometrically thick, optically thin, advection dominated flow. The density is taken to be constant in θ , so $\rho = \rho_0 r^{-\frac{3}{2}}$.

2.3 Bipolar outflow

Outflow solutions have been considered by several authors (e.g. Xu and Chen 1997; Quartaert and Narayan 1999; Blandford and Begelman 1999). Perna et al. (2000) give approximate analytic expressions. We use their solutions with density independent of angle and with winds of $p = \frac{1}{2}$, where p is defined so that $M \propto r^p$. The equations then become

$$\rho = \rho_0 r^{-\frac{3}{2}}, \quad (7)$$

$$v_r = \frac{3\alpha}{5+2\epsilon} r\Omega_K(r)[\cos 2\theta + \cos^2 \theta], \quad (8)$$

$$v_\theta = \frac{3\alpha}{5+2\epsilon} \frac{r\Omega_K(r)}{4} \sin 2\theta, \quad (9)$$

$$v_\phi = \left(\frac{2\epsilon}{5+2\epsilon} \right)^{\frac{1}{2}} r\Omega_K(r) \sin \theta, \quad (10)$$

$$c_s = \frac{r\Omega_K(r)}{\sqrt{5+2\epsilon}} \sqrt{2 - \epsilon \cos^2 \theta}. \quad (11)$$

3 CALCULATION OF THE LINE PROFILE

3.1 Total flux

The total flux observed at frequency ν is given by

$$F(\nu) = \int \delta(\nu - \nu_0(\mathbf{r})) f(\mathbf{r}, \nu) d^3r, \quad (12)$$

where $\nu_0(\mathbf{r})$ is the observed frequency of flux emitted from \mathbf{r} , calculated below, and $I(\mathbf{r}, \nu)$ is given by

$$f(\mathbf{r}, \nu) = \left[\frac{\nu}{\nu_e} \right]^3 f_{out}(\mathbf{r}, \mathbf{c}(\mathbf{r})) V(\mathbf{r}), \quad (13)$$

where $\left[\frac{\nu}{\nu_e} \right]^3$ is the relativistic correction to the flux, with the frequency of emission, $\nu_e = 6.4\text{keV}$ for the iron line. $f_{out}(\mathbf{r}, \mathbf{c}(\mathbf{r}))$ is the flux reprocessed and re-emitted by clouds at \mathbf{r} in the direction $\mathbf{c}(\mathbf{r})$, defined such that the photons reach the observer (calculated below). Finally, $V(\mathbf{r})$ is the *visibility function* which gives the probability of flux from \mathbf{r} reaching the observer without being intercepted by an optically thick cloud. It is given by

$$V(\mathbf{r}) = \max(1 - P(\mathbf{r}), 0), \quad (14)$$

with the probability of interception

$$P(\mathbf{r}_0) = \int_a^b n_c(\mathbf{r}(\lambda)) A(\mathbf{r}(\lambda), \frac{d\mathbf{r}}{d\lambda}) \left| \frac{d\mathbf{r}}{d\lambda} \right| d\lambda, \quad (15)$$

where $\mathbf{r}(a) = \mathbf{r}_0$, the position of emission, and $\mathbf{r}(b) = \mathbf{r}_{\text{obs}}$, the position of the observer, and λ parametrises the path of the photon. $n_c(\mathbf{r})$ is the number density of clouds in the disc and $A(\mathbf{r}, \frac{d\mathbf{r}}{d\lambda})$ is the cross sectional area of the clouds at \mathbf{r} , as seen by a photon travelling in direction $\frac{d\mathbf{r}}{d\lambda}$. These quantities are discussed below. The visibility function must also include the possibility of photons falling into the event horizon.

The dimensions of the disc are taken to be $6 \leq r \leq 300$, $0 \leq \theta \leq \pi$ and $0 \leq \phi < 2\pi$, although there will not necessarily be a significant number density of clouds throughout this whole region (because the number density of particles in the disc itself gets smaller for larger r and, depending on the thermodynamic parameter ϵ , gets smaller further from the equatorial plane). Also, the volume element has a general relativistic correction, so

$$d^3r = \frac{dr}{\sqrt{1 - \frac{2}{r}}} r^2 \sin \theta d\theta d\phi. \quad (16)$$

3.2 Photon paths

We use paths in the Schwarzschild metric, approximated by a first order perturbation. We take units with $c = G = 1$ and take the mass of the central object to be $M = 1$. Note that in this section \mathbf{r} is the position of the photon travelling from the cloud to the observer, and \mathbf{r}_0 is the position of the emitting cloud in the disc. We write $r_0 = |\mathbf{r}_0|$ and $r = |\mathbf{r}|$.

First order perturbation of the Schwarzschild null geodesic equations gives the photon path to be

$$\frac{1}{r(\Phi)} = \frac{\sin \Phi}{2R} + \frac{1 + C \cos \Phi + \cos^2 \Phi}{4R^2} + \mathcal{O}(\frac{1}{R^3}). \quad (17)$$

Where R and C are constants, $r(\Phi)$ is the radial distance from the origin at the central object and Φ is a polar angle on the plane of the trajectory. The trajectory plane is defined by the origin, the direction to the observer, $\hat{\mathbf{n}}$, and the initial position vector \mathbf{r}_0 .

The boundary conditions are that the photon starts at (r_0, Φ_0) and ends at $(\infty, \Phi_{\text{obs}})$, written in (r, Φ) coordinates on the trajectory plane. The boundary conditions are simplified if we choose the axis on the trajectory plane that defines Φ to be in the direction towards the observer, $\hat{\mathbf{n}}$, so that $\Phi_{\text{obs}} = 0$. The constants are then given by

$$C = -2, \quad (18)$$

$$R^\pm = \frac{r_0 \sin \Phi_0}{4} \pm \frac{r_0}{4} \sqrt{\sin^2 \Phi_0 + \frac{4}{r_0} (1 - \cos \Phi_0)^2}. \quad (19)$$

Note that the minus sign case results in R negative, which is not physical, so we take the positive solution. Selecting this single path is effectively not considering orbits that loop around the central hole one or more times, consistent with the perturbative approach.

With this choice of axis, Φ_0 is given by

$$\cos \Phi_0 = \frac{\mathbf{r}_0 \cdot \hat{\mathbf{n}}}{r_0}. \quad (20)$$

In principle, there could be a problem inverting this expression due to ambiguities in the definition of the inverse cosine. However, these are avoided if we take the other axis on the trajectory plane to be $\frac{\mathbf{r}_0 - (\mathbf{r}_0 \cdot \hat{\mathbf{n}})\hat{\mathbf{n}}}{r_0}$. This vector, orthogonal to $\hat{\mathbf{n}}$, is such that \mathbf{r}_0 has positive component in this direction. Therefore, we may take $\Phi_0 \in [0, \pi]$ with no ambiguities and the trajectory is given by

$$\mathbf{r}(\Phi) = r(\Phi) \left[\cos \Phi \hat{\mathbf{n}} + \sin \Phi \frac{\mathbf{r}_0 - (\mathbf{r}_0 \cdot \hat{\mathbf{n}})\hat{\mathbf{n}}}{r_0} \right]. \quad (21)$$

This gives the probability of interception as

$$P(\mathbf{r}_0) = \int_0^{\cos^{-1} \frac{\mathbf{r}_0 \cdot \hat{\mathbf{n}}}{r_0}} n(\mathbf{r}(\Phi)) A(\mathbf{r}(\Phi), -\frac{d\mathbf{r}}{d\Phi} \left| \frac{d\mathbf{r}}{d\Phi} \right|) d\Phi, \quad (22)$$

and the angle of emission is given by

$$\mathbf{c}(\mathbf{r}_0) = -\frac{d\mathbf{r}}{d\Phi}(\Phi = \Phi_0). \quad (23)$$

The minus sign in the last two equations results because the photon travels in the direction of decreasing Φ .

3.3 Frequency shifts

The observed frequency is given in terms of the emitted frequency by

$$\nu_0 = \nu_e \frac{(p_\mu U^\mu)_{obs}}{(p_\mu U^\mu)_{em}}, \quad (24)$$

where p^μ is the photon 4-momentum and U^μ is the 4-velocity of the emitter or observer. We employ general relativity in the Schwarzschild metric, $g_{\mu\nu}$. Write $p^\mu = (p^t, \mathbf{p})^\mu$, and $U^\mu = \frac{dt}{d\tau}(1, \mathbf{u})^\mu$. The time component of photon 4-momentum in the Schwarzschild metric is

$$p^t = \frac{E}{1 - \frac{2}{r}}, \quad (25)$$

Where E is constant along the photon trajectory. So requiring the photon 4-momentum to be null, $g_{\mu\nu} p^\mu p^\nu = 0$, gives $\mathbf{p}^2 = g_{ij} p^i p^j = \frac{E^2}{1 - \frac{2}{r}}$ to be the appropriate normalisation for the spatial components. In the Schwarzschild metric, we have

$$\frac{dt}{d\tau} = \frac{1}{\sqrt{1 - \frac{2}{r} - \frac{u_r^2}{1 - \frac{2}{r}} - u_\theta^2 - u_\phi^2}}. \quad (26)$$

By definition,

$$p_\mu U^\mu = g_{\mu\nu} p^\mu U^\nu, \quad (27)$$

where the observer has $\mathbf{u}_{obs} = 0$ and $r_{obs} \rightarrow \infty$. The emitter has $\mathbf{p}_{em} \propto \mathbf{c}$ and $r_{em} = r_0$. Putting all this into (24) gives

$$\nu_0(\mathbf{r}_0) = \frac{\nu_e \sqrt{1 - \frac{2}{r_0} - \frac{u_r^2(\mathbf{r}_0)}{1 - \frac{2}{r_0}} - u_\theta^2(\mathbf{r}_0) - u_\phi^2(\mathbf{r}_0)}}{1 - \frac{c_r(\mathbf{r}_0)u_r(\mathbf{r}_0)}{1 - \frac{2}{r_0}} - c_\theta(\mathbf{r}_0)u_\theta(\mathbf{r}_0) - c_\phi(\mathbf{r}_0)u_\phi(\mathbf{r}_0)}. \quad (28)$$

Here $\mathbf{u}(\mathbf{r}_0)$ is the velocity of the clouds at \mathbf{r}_0 . We take the velocity of clouds to trace the velocity of the fluid in the disc. This is given by one of the disc motions described in the previous section.

3.4 Distribution and sizes of clouds

For simplicity, we will assume that all of the clouds are spherical. The cross section is then independent of a photon's direction of approach. If we consider clouds with the same total number of particles, this allows us to write

$$A(\mathbf{r}) \propto V^{\frac{2}{3}}(\mathbf{r}) \propto \frac{1}{n_{p,c}^{\frac{3}{2}}(\mathbf{r})}, \quad (29)$$

where $n_{p,c}$ is the number density of particles in the cloud.

Thermal equilibrium gives a relation between the number density of particles in the cloud and the number density of particles in the disc, n ,

$$n_{p,c}(\mathbf{r}) = \frac{n(\mathbf{r})T(\mathbf{r})}{T_c(\mathbf{r})}, \quad (30)$$

where T and T_c are the temperatures of protons in the disc and the clouds, respectively. We take the temperature of the clouds to be the same everywhere - around $T_c = 10^5$ K (Kuncic et al, 1996), although the actual value will be absorbed into an overall constant - and find the temperature of the disc from the sound speed, c_s , as

$$T(\mathbf{r}) = \frac{m_p c_s^2(\mathbf{r})}{k}, \quad (31)$$

where k is Boltzmann's constant and m_p is the mass of the proton. This gives us the cross section

$$A(\mathbf{r}) \propto \left[\frac{kT_c}{m_p n(\mathbf{r})c_s^2(\mathbf{r})} \right]^{\frac{2}{3}} \propto \left[\frac{1}{\rho(\mathbf{r})c_s^2(\mathbf{r})} \right]^{\frac{2}{3}}. \quad (32)$$

We take $\rho(\mathbf{r})$ and $c_s^2(\mathbf{r})$ from the solutions of the previous section. The expression should be normalised by the cross section of the clouds being around 10^{10} cm² at the innermost radius (Kuncic et al., 1996), however in practice we can absorb this constant into the constant Γ , defined below.

The various assumptions above about the cloud structure (constant number of particles, constant temperature) result in clouds with size growing strongly with r , as $r^{\frac{5}{3}}$. Combined with the radial dependence of the flux emission (discussed in more detail below), this results in profiles dominated by the outer disc regions. We also want to consider more general radial dependencies, where profiles are dominated by the central regions. We therefore add the term r^{-g} , to the cloud cross section, where generally g is a small positive number. This has a somewhat analogous rôle to the r^{-q} term in the standard thin disc models (Fabian et al. 1989), although has a physically different origin. The final expression is then

$$A(\mathbf{r}) \propto \left[\frac{1}{\rho(\mathbf{r})c_s^2(\mathbf{r})} \right]^{\frac{2}{3}} r^{-g}. \quad (33)$$

We take the number density of clouds to trace the number density of protons in the disc, hence

$$n_c(\mathbf{r}) = \Gamma \rho(\mathbf{r}). \quad (34)$$

The constant of proportionality, Γ , will determine the degree of shadowing by optically thick clouds. The probability of obscuration, $P(\mathbf{r})$, with maximal value 1, is proportional to Γ .

3.5 Emitted flux

We take the emitted flux to be proportional to the flux illuminating the clouds, f_{in} , the number density of the clouds, and the cross section of the clouds.

We take two contributions to the flux illuminating the clouds, a central illumination (e.g. due primarily to synchrotron radiation in the innermost regions of the flow for ADAFs Mahadevan 1997) an X-ray bath throughout the disc (due to Bremsstrahlung radiation). The central illumination falls off as $\frac{1}{r^2}$ and the Bremsstrahlung is proportional to the square of the number density of particles in the disc. So the emitted flux is given by

$$f_{out}(\mathbf{r}, \mathbf{c}(\mathbf{r})) \propto n_c(\mathbf{r}) A(\mathbf{r}) f_{in}(\mathbf{r}) \\ \propto \rho A(\mathbf{r})^{\frac{2}{3}} \left[\frac{A \max(-\hat{\mathbf{r}} \cdot \hat{\mathbf{c}}(\mathbf{r}), 0)}{r^2} V_p(\mathbf{r}) + B \rho^2 \right]. \quad (35)$$

Here A and B are constants determining the relative importance of central radiation and the X-ray bath. They will depend on the mass accretion rate of the system (Mahadevan 1997) and also the geometry of the clouds. The $\max(-\hat{\mathbf{r}} \cdot \hat{\mathbf{c}}(\mathbf{r}), 0)$ term contains the information that only the side of the cloud facing the centre of the disc is illuminated by the central flux. Hence, the corresponding reprocessed flux is only visible for clouds on the far side of the hole with respect to the observer, and the amount of flux seen by the observer decreases as the illuminated side of the clouds becomes more edge on to the observer. $V_p(\mathbf{r})$ is the primary visibility function, analogous to the visibility function described earlier, giving the probability of photons emitted from the central regions reaching the cloud without being obscured by intermediate clouds. Fortunately, the photon paths from the central illumination are radial and so the integration of equation 15 becomes analytically tractable, using appropriate expressions for the cross sections and cloud number densities.

To give some visualisation of the processes involved, we will consider five cross sections of the disc at different heights above the equatorial plane, as shown in Fig. 1. For each cross section, we compute a frequency map and a visibility map for both a centrally illuminated (synchrotron dominated) case and an X-ray bath (Bremsstrahlung dominated) case. The disc visualised is a self-similar ADAF disc with $\epsilon = 0.1$ and $\alpha = 0.35$, viewed at 60 degrees. The results are shown in Fig. 2, in which the observer is situated to the right.

Some thought reveals that the plots of Fig. 2 make sense physically, and the qualitative features deserve some further comments. The redshift map of the equatorial is different in two respects from the standard redshift maps of thin discs. Firstly, the regions of largest Doppler shift are rotated slightly with respect to the observer. This is because the radial motion is of similar magnitude to the rotational motion. Secondly, gravitational redshift is much more dominant. This is because the velocities are significantly less than the Keplerian velocities of a thin disc (see comments in §2.1).

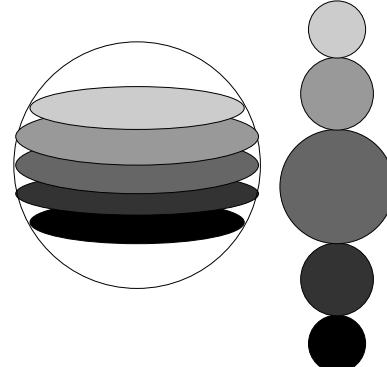


Figure 1: The cross sections of the disc used in Fig. 2.

As we would expect, the redshifts become less pronounced as we move away from the equatorial plane.

The visibility in the centrally illuminated case is a superposition of the visibility in the X-ray bath case with the primary visibility. The primary visibility implies that the observer can only see clouds on the far side of the hole (hence there is more obscuration on the top part of the disc than the bottom part) and that the more edge-on clouds appear less illuminated.

The visibility in the X-ray bath case is determined by the size and number density of clouds as well as the length of the trajectory through the clouds. This results in the central regions being the most obscured because the disc under consideration has $g = 1.5$, which means the cloud number density times cross section is largest in the central regions. Also, the bottom regions are more obscured than the top regions because they are further from the observer.

4 LINE PROFILES

Discs were considered (*i*) at two or three different inclinations (15, 30 and 60 degrees, or some subset thereof), (*ii*) once with shadowing (Γ finite) and once without ($\Gamma = 0$), and (*iii*) once with the profile dominated by the outer regions ($g = 0$) and once with the profile dominated by inner regions ($g = 1.5$). All discs have $\alpha = 0.35$.

4.1 Self-similar ADAF profiles

We consider three ADAF discs. The first has $\epsilon = 0.1$, hence the density dependence is essentially spherically symmetric. We take this disc to be dominated by central illumination (i.e. $A = 10, B = 1$ in equation 35). The second disc also has $\epsilon = 0.1$ but is dominated by the X-ray bath (i.e. $A = 1, B = 100$). The third has $\epsilon = 10$, hence the density is concentrated within around 30 degrees of θ on each side of the equatorial plane. We take this disc to be dominated by central illumination.

A striking feature of the profiles from the two $\epsilon = 0.1$ ADAF discs considered, Figs. 3 and 4, is the lack of significant dependence on the inclination angle (compare to the profiles from flat thin discs in, e.g. Fabian et al. 1989, which show a strong inclination dependence). This is because the velocities given by equations 2-4 have magnitudes smaller than the Keplerian velocities of thin discs and so extreme

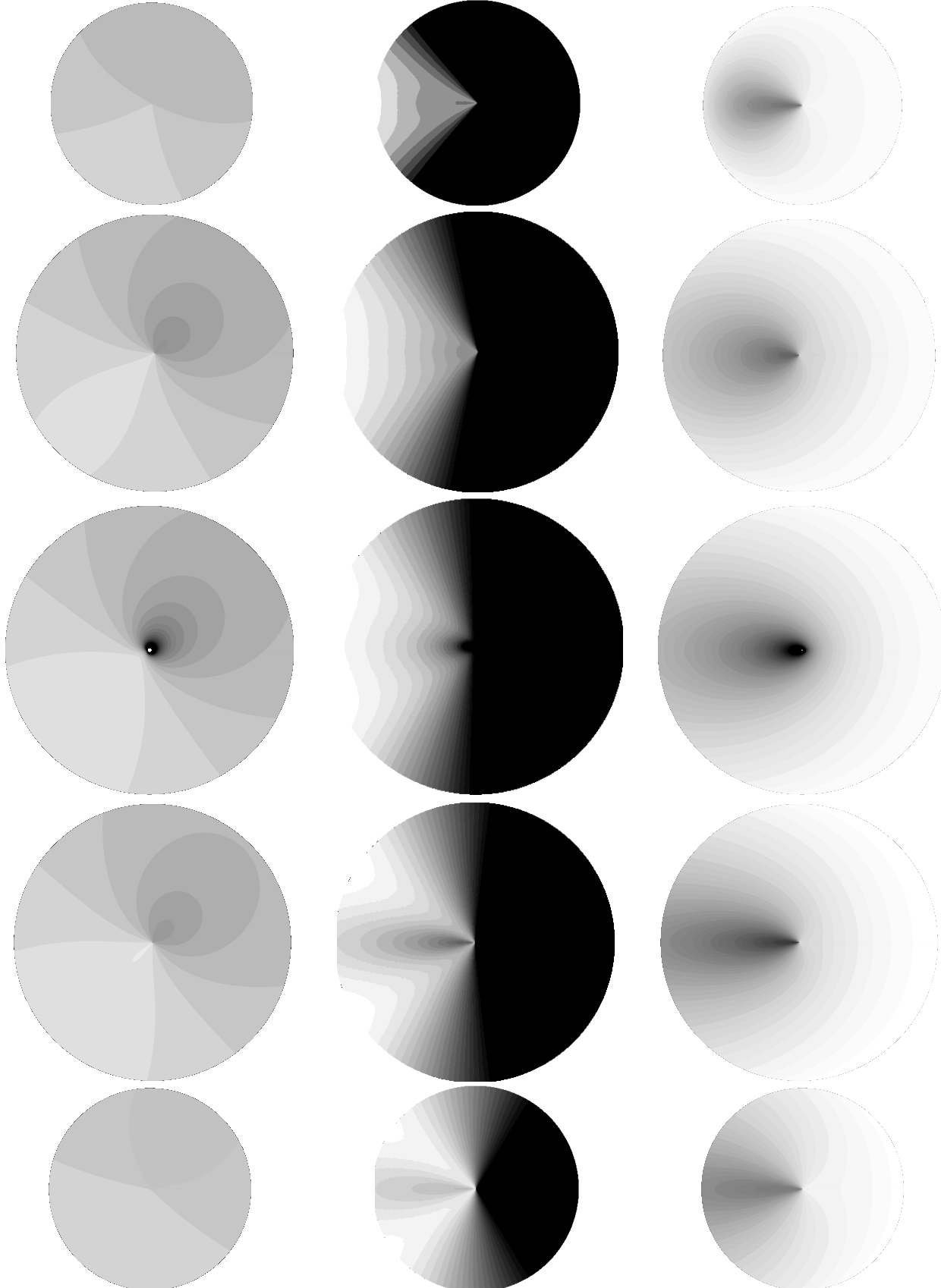


Figure 2: From top to bottom, cross sections of a disc at heights of $0.7r_{out}$, $0.25r_{out}$, 0 , $-0.25r_{out}$ and $-0.7r_{out}$ vertically relative to the equatorial plane, drawn to scale. The left column shows redshifts (darker shows more redshifted), the central column shows visibility in the centrally illuminated (synchrotron dominated) case and the right column shows visibility in an X-ray bath (Bremsstrahlung dominated) case. White regions are totally unshadowed and black regions are totally shadowed. The observer is to the right and the disc is rotating counter clockwise.

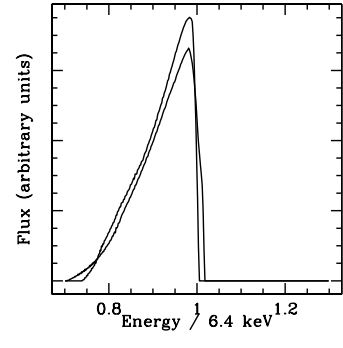
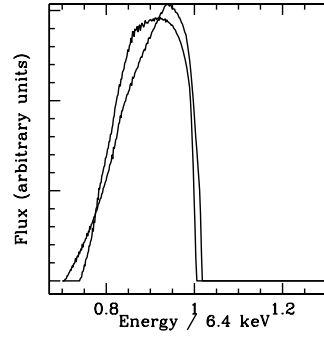
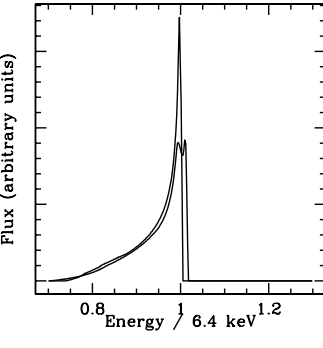
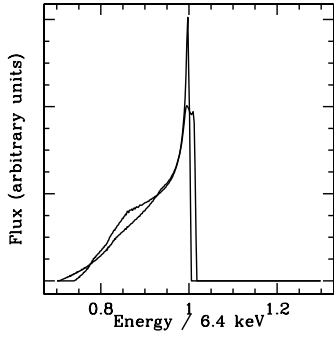
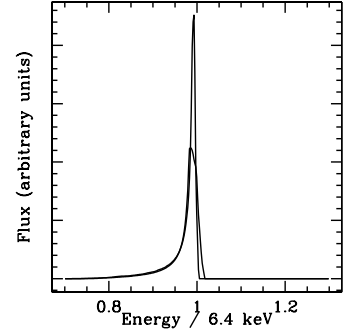
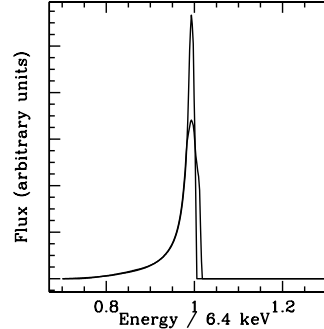
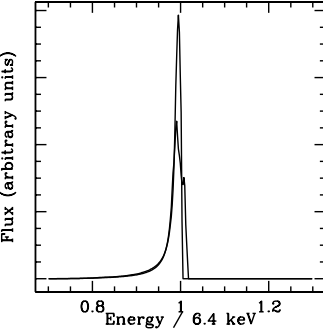
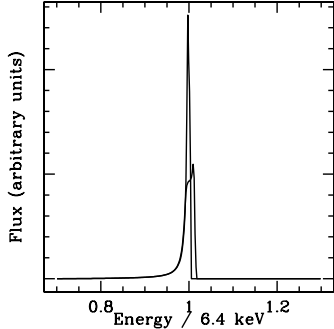


Figure 3: Profiles from an ADAF disc with $\epsilon = 0.1$. Central illumination dominated ($A = 10, B = 1$). Left to right: non-shadowed and shadowed. Top to bottom: $g = 0$ (outer region dominated) and $g = 1.5$ (inner region dominated). Each plot shows profiles for inclinations of 15 and 60 degrees, plotted to scale (i.e. not separately normalised). The profile with the higher peak is at 15 degrees.

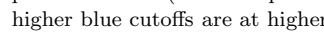
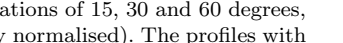
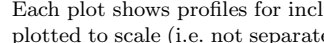
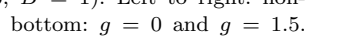
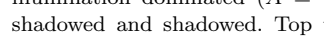
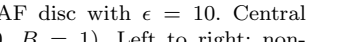
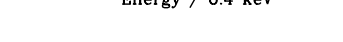
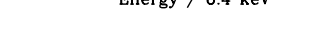
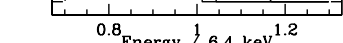
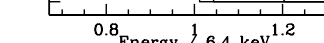
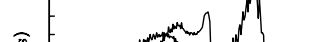
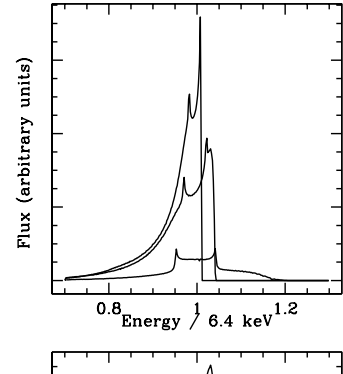
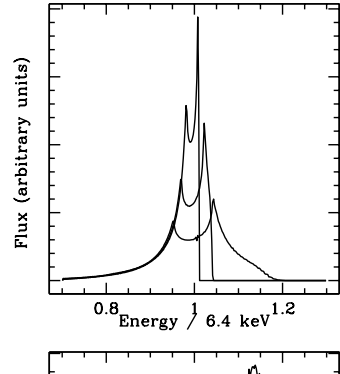
blue Doppler shifts do not appear. There is more blue-shifted flux for the higher inclination discs, which is why the peak very near the rest frequency is lower in the higher inclination discs.

The discs with $g = 1.5$ have profiles dominated by flux from the inner regions, which explains the greater presence of gravitationally redshifted flux. This is most notable in the X-ray bath case of Fig. 4 because here there is a contribution from Doppler redshifted flux which is not so visible in the centrally illuminated case. See Fig. 2 for how the shadowings and redshifts interact. The fact that $v_r \approx v_\theta$ in the discs of Figs. 3 & 4 is important because it rotates the most Doppler redshifted region into the less visible sector of the disc for the centrally illuminated case, Fig. 3.

The most notable feature of the profiles from the $\epsilon = 10$ ADAF disc, in Fig. 5, is that cases with $g = 0$ are of virtually identical form as the standard thin disc profiles, and show the same inclination dependence as the thin discs! This is not too surprising because the velocities of equations 2-4 give a magnitude very close the Keplerian magnitude and the angular motion is more important than the radial motion.

The profiles with $g = 1.5$ are dominated by emission from the central regions, which results in the large amounts of red and blue shifted flux due to Doppler and gravitational effects.

Figure 4: Profiles from an ADAF disc with $\epsilon = 0.1$. X-ray bath dominated ($A = 1, B = 100$). Left to right: non-shadowed and shadowed. Top to bottom: $g = 0$ and $g = 1.5$. Each plot shows profiles for inclinations of 15 and 60 degrees, plotted to scale (i.e. not separately normalised). The profile with the higher blue cutoff is at 60 degrees.



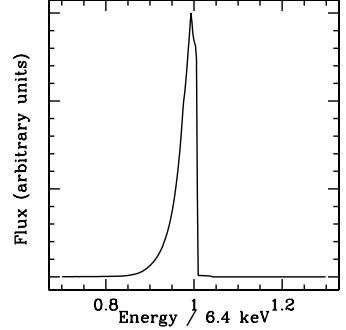
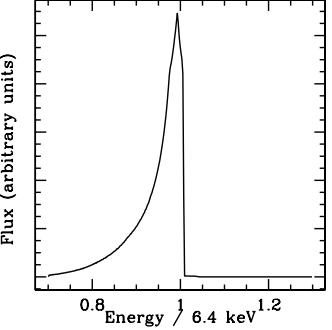
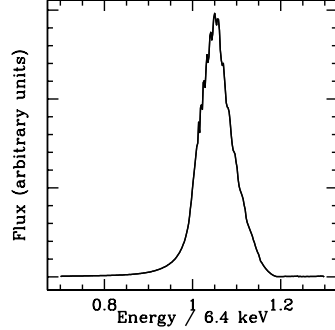
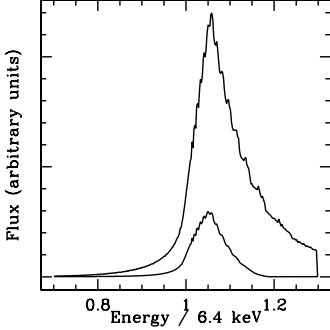
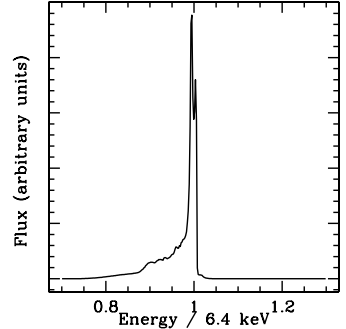
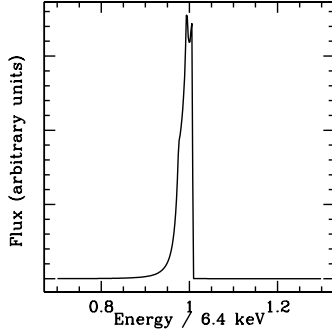
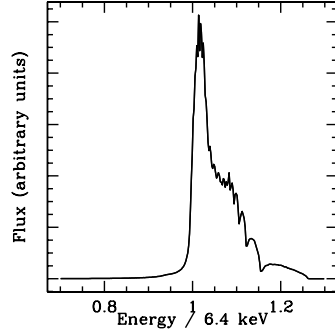
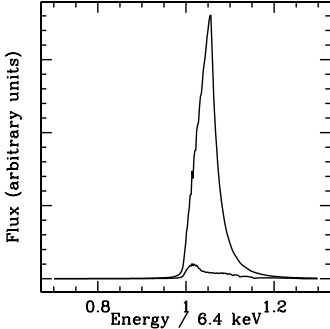


Figure 6: Profiles from a radially infalling disc. Central illumination dominated ($A = 10$, $B = 1$). Left to right: non-shadowed+shadowed (to scale) and shadowed (scaled up). Top to bottom: $g = 0$ and $g = 1.5$.

4.2 Radial infall profiles

We consider a radially infalling disc dominated by central illumination. The profile is independent of inclination because of the spherical symmetry, so only one inclination angle is considered. The profiles are shown in Fig.6. To show explicitly the effect of shadowing, the non-shadowed profiles are plotted to scale with the shadowed profiles in the left column.

The profiles show a significant amount of blueshifted flux and little redshifted flux. This is the immediate consequence of the central illumination which means the blobs falling inwards towards the observer are visible, whilst those falling inwards away from the observer are illuminated on the side obscured from the observer. In the case where the profile is dominated by contributions from the central regions ($g = 1.5$), we see a gravitational redshift and more blueshift from the fast inner flow.

4.3 Outflow profiles

We consider a disc with the bipolar outflow solutions of equations 7 to 11. The disc has $\epsilon = 0.1$ and is dominated by central illumination.

The profiles are very similar to those generated by the ADAF solutions without outflows. Here we show the 30 degree inclination profiles, but the profiles for different inclinations are very similar, as for the ADAF cases. The double peak for the outer region dominated case is seen in the top row of Fig. 7. The redshift dominates the flux in both cases. This is because of the gravitational redshift, and because the use of central illumination means that the observer primar-

Figure 7: Profiles from a bipolar outflow disc. Central illumination dominated ($A = 10$, $B = 1$). Left to right: non-shadowed+shadowed (to scale) and shadowed (scaled up). Top to bottom: $g = 0$ and $g = 1.5$. Inclination of 30 degrees.

ily sees emission from the clouds moving away from his/her line of sight. This is opposite to the radial infall case.

5 DISCUSSION AND CONCLUSION

We have considered a model in which cold, dense clouds are embedded in an otherwise optically thin, but geometrically thick accretion flow. Assuming these clouds reprocess primary X-ray emission from a central source and an X-ray bath, we have computed the expected fluorescent iron line profiles. This is a different scenario to the standard calculation of line profiles from thin, flat discs.

We considered various solutions for the dynamics of the disc: ADAFs, pure radial infall models, and bipolar outflows. We allow these solutions to specify the velocity, number density and size of the clouds at different points of the engine. In calculating the line profiles, a new effect compared to the thin disc models is the obscuration of flux by the clouds themselves, which are optically thick.

Many of the resulting line profiles are similar to those from thin disc models, suggesting that thin discs do not provide a unique model that is able to reproduce observations of iron line profiles. This suggests that cloud models warrant further study. Previous work has focused primarily on the X-ray continuum (Sivron and Tsuruta 1993; Bond and Matsumura 1993; Nandra and George 1994; Collin-Souffrin et al. 1996) but there has been little modelling of the relativistic iron fluorescent line for the cloud model. Karas et al. 2000 considered non-relativistic profiles with large clouds at one radius.

A further incentive to consider thick disks with embedded clouds is that they may help resolve problems arising in

thin disc modelling which relate to the inclination of discs and the reprocessed fraction. This includes the puzzling preference for low inclinations for Seyfert 2s (Turner et al. 1998), some incongruences between inferred inclinations from iron line modelling and those determined from other methods (Nishiura et al. 1998; Sulentic et al. 1998a; Wang et al. 1999), and the observed reprocessed fraction appearing to be too low and/or uncorrelated with line width (e.g. Lee et al. 2000; Chiang et al. 2000; Weaver 2000; Sulentic et al. 1998b). In this regard, we find that many of our embedded cloud, thick disc profiles (modelled with ADAF type flows) are relatively insensitive to the inclination angle because a significant pressure support means that the bulk velocities are smaller than the Keplerian values.

This latter feature also means that many of our profiles have sharp blue cut-offs because they are dominated by the gravitational redshift. Whether the sharp blue cut-off remains true in the Kerr case, where the disc extends closer to central hole and hence can acquire greater velocities should be investigated. Note that this will also depend fundamentally on the innermost radius at which the reprocessing clouds can survive. A thick geometry can also allow a wider range of reprocessed fractions, depending on the cloud distribution and amount of obscuration.

To summarise, the embedded cloud+ thick disc model allows a wider range of disc flow solutions to show reprocessed X-rays lines, and highlights how an alternative geometry can produce profiles similar to those from thin discs. The model can also lead to profiles with different properties to those of the thin discs, such as less sensitivity to inclination angle. As such, we suggest the cloud model deserves further investigation. This would include more consideration of the mechanisms of cloud formation and sizes, generalisation to the Kerr metric, and application to specific sources.

ACKNOWLEDGEMENTS

Thanks to Clovis Peres for many fruitful discussions and early collaborations on this subject. SAH acknowledges the hospitality of the University of Rochester and the REU program. EB acknowledges partial support from DOE grant DE-FG02-00ER54600.

REFERENCES

Blackman E.G., 1999, MNRAS, 306, L25
 Blandford R.D. & Begelman M.C., 1999, MNRAS, 303, L1
 Bond I.A. & Matsuoka M., 1993, MNRAS, 265, 619
 Bondi H., 1952, MNRAS, 184, 53
 Cao X.W. & Zhang J.L., 1992, ChA&A, 16:1, 17
 Celotti A., Fabian A.C. & Rees, M.J., 1992, MNRAS, 255, 419
 Collin-Souffrin S., Czerny B., Dumont A-M. & Zycki P.T., 1996, A&A, 314, 393
 Fabian A.C., Rees M.J., Stella L. & White N.E., 1989, MNRAS, 238, 729
 Fabian A.C., Iwasawa K., Reynolds C.S. & Young A.J., 2000, PASP, in press
 Ferland G.J. & Rees M.J., 1988, ApJ, 332, 141
 George A.M. & Fabian A.C., 1991, MNRAS, 249, 352
 Guilbert P.W. & Rees M.J., 1988, MNRAS, 233, 475
 Hartnoll S.A. & Blackman E.G., 2000, MNRAS, 317, 880
 Karas V., Czerny B., Abramart A. & Abramowicz M. A., 2000, MNRAS, in press
 Kuncic Z., Blackman E.G. & Rees M.J., 1996, MNRAS, 283, 1322
 Laor A., 1991, ApJ, 376, 90
 Lee J.. Fabian A.C., Reynolds C.S., Brandt W.N. & Iwasawa K., 2000, MNRAS, in press
 Mahadevan R., 1997, ApJ, 477, 585
 Nandra K. & George I.M., 1994, MNRAS, 267, 974
 Nandra K., George I.M., Mushotzky R.F., Turner T.J. & Yaqoob T., 1997, ApJ, 477, 602
 Nandra K., 2000, astro-ph/0007356
 Narayan R. & Yi I., 1994, ApJ, 428, L13
 Narayan R. & Yi I., 1995, ApJ, 444, 231
 Narayan R., Mahadevan R. & Quataet E., in *The Theory of Black Hole Accretion Discs*, eds. Abramowicz M.A., Bjornsson G. & Pringle J.E., Cambridge University Press, 1998, p. 148
 Narayan R., Igumenshchev I.V. & Abramowicz M.A., 2000, ApJ, in press, astro-ph/9912449
 Nishiura S., Murayama T. & Taniguchi Y., 1998, PASJ, 50, 31
 Pariev V.I. & Bromley B.C., 1998, ApJ, 508, 590
 Perna R., Raymond J. & Narayan R., 2000, ApJ, in press
 Quataert E. & Narayan R., 1999, ApJ, 520, 298
 Quataert E., Gruzinov A., 2000, ApJ, 539, 809
 Rees M.J., 1984, ARA&A, 22, 417
 Rees M.J., Begelman M.C., Blandford R.D. & Phinney E.S., 1982, Nature 295 17.
 Sivron R. & Tsuruta S., 1993, ApJ, 402, 420
 Sulentic J.W., Marziani P., Zwitter, T., Calvini M. & Dultzin-Hacyan D., 1998a, ApJ, 501, 54
 Sulentic J.W., Marziani P. & Calvani M., 1998b, ApJ, 497, L65
 Tanaka Y. et al., 1995, Nature, 375, 659
 Tanaka Y. 2000, in *Highly Energetic Processes and Mechanisms for Emission from Astrophysical Plasmas*, proc. IAU Symp 195, P.C.H. Martens, S.Tsuruta, M.A. Weber eds., Astron. Soc. of the Pacific., San Francisco, p37.
 Turner T.J., George I.M., Nandra K. & Mushotzky R.F., 1998, ApJ, 493, 91
 Wang J.X., Zhou Y.Y. & Wang T.G., 1999, ApJ, 523, L129
 Wang J.X., Zhou Y.Y., Yuan Y., Cao X. & Wu M., 2000, ApJ, in press
 Weaver K.A., Reynolds C.S., 1998, ApJ, 503, L39
 Weaver K.A., in *Proceedings of X-ray Astronomy '99 - Stellar Endpoints, AGN and the Diffuse Background*, eds. Malagutti G., Palumbo G. & White N., Gordon & Beach (Singapore), 2000
 Xu G. & Chen X., 1997, ApJ, 489, L29